

pubs.acs.org/JPCB Article

Electronic Structure of de Novo Peptide ACC-Hex from First Principles

D. Kirk Lewis, Younghoon Oh, Luke Nambi Mohanam, Michał Wierzbicki, Nicole L. Ing, Lei Gu, Allon Hochbaum, Ruqian Wu, Qiang Cui, and Sahar Sharifzadeh*



Cite This: J. Phys. Chem. B 2022, 126, 4289-4298



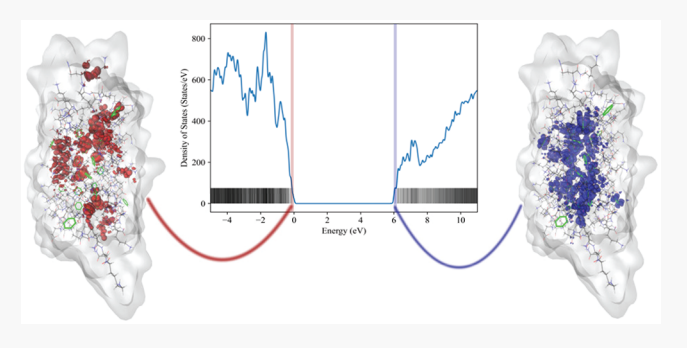
ACCESS I

Metrics & More

Article Recommendations

Supporting Information

ABSTRACT: Proteins are promising components for bioelectronic devices due in part to their biocompatibility, flexibility, and chemical diversity, which enable tuning of material properties. Indeed, an increasingly broad range of conductive protein supramolecular materials have been reported. However, due to their structural and environmental complexity, the electronic structure, and hence conductivity, of protein assemblies is not well-understood. Here we perform an all-atom simulation of the physical and electronic structure of a recently synthesized self-assembled peptide antiparallel coiled-coil hexamer, ACC-Hex. Using classical molecular dynamics and first-principles density functional theory, we examine the interactions of each peptide,



containing phenylalanine residues along a hydrophobic core, to form a hexamer structure. We find that while frontier electronic orbitals are composed of phenylalanine, the peptide backbone and remaining residues, including those influenced by solvent, also contribute to the electronic density. Additionally, by studying dimers extracted from the hexamer, we show that structural distortions due to atomic fluctuations significantly impact the electronic structure of the peptide bundle. These results indicate that it is necessary to consider the full atomistic picture when using the electronic structure of supramolecular protein complexes to predict electronic properties.

1. INTRODUCTION

Peptides and proteins are promising building blocks for bioelectronic materials that interface biological systems and synthetic devices. Natural assemblies of proteins have been recently discovered that conduct charge over a range of length scales. 1-4 These assemblies represent soft materials capable of self-assembling into nanostructures with highly tunable properties, 5-8 including access to a range of dynamic assembly pathways and transient structures. 9,10 Certain peptides and proteins exhibit excellent biocompatibility in terms of eliciting a minimal immune response, 11-13 the ability to be safely degraded/absorbed by the body after use, 14,15 and controllable degradation kinetics. 16-18 Additionally, the chemical diversity of peptides allows for highly optimized enzyme immobilization 19,20 and cellular interfacing. 21-23 Many natural and synthetic proteins and peptides are also capable of selfassembling into supramolecular nanostructures, such as sheets, wires, and tubes. 24,25 High aspect ratio structures offer additional benefits for interfacing with biology, 26,27 and the diversity of self-assembly motifs present in protein structure promises to mitigate the difficulties and costs associated with their nanofabrication by traditional approaches.²⁸

What is currently unclear is why proteins or peptides should be good electronic conductors. Electron transfer experiments suggest that amino acids between donor—acceptor centers in metalloenzymes make a relatively poor tunneling medium. ^{29,30} Natural^{1,2} and synthetic^{31,32} protein and peptide supramolecular materials exhibit electronic conductivity, but the chemical and structural features supporting long-range electron transport in these materials are poorly understood.

To better understand conductivity in bioelectronic materials, models of electron conductivity have been developed. These models make approximations, often parametrizing the system to reduce the complexity of the problem at hand. For systems with spatially delocalized charge carriers, coherent band-like transport models capture the electron transport behavior, ³³ while for systems with spatially localized charge carriers, incoherent electron transfer between localized ^{34–36} or delocalized states ^{37,38} may be more suitable. For many systems, the conductivity is best described by a mixed coherent—incoherent transport model, ^{39,40} where a basis of electronically

Received: April 6, 2022 Revised: May 20, 2022 Published: June 7, 2022





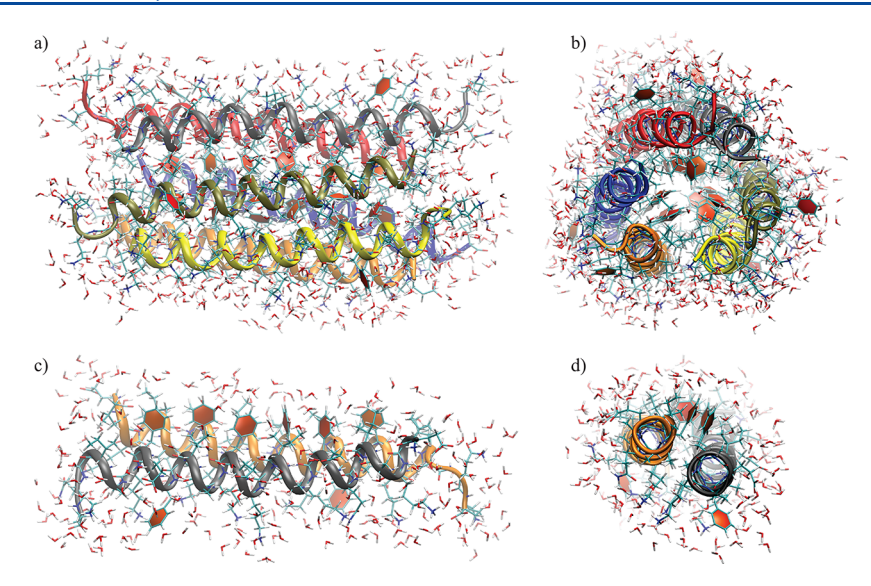


Figure 1. Antiparallel coiled-coil hexamer ACC-Hex surrounded by a 2.8 Å thick water shell, viewed (a) perpendicular to and (b) parallel to its long axis. One of the three peptide dimers composing ACC-Hex, surrounded by a 2.8 Å thick water shell, (c) perpendicular and (d) parallel to its long axis.

coupled (i.e., electronically diabatic) localized charge carrier sites is able to describe the delocalization and localization of the charge carrier density matrix over time. The conductivity regime is determined by the electronic and physical structure of the assembly.^{30,41} The bandgap (energy difference between the highest occupied molecular orbital (HOMO) and lowest unoccupied molecular orbital (LUMO)), the bandwidth (or energy level spacing), and the localization of orbitals will significantly impact the conductivity regime and efficiency of long-range electron transport. The energetics and coherence of electronic states are in turn dependent on the physical structure of the system; for example, the distance and orientation between amino acids, 41 and the presence and pH of the solution 42-44 can modify electronic coupling and the bandgap. Thus, it is necessary to understand the relationship between atomic structure, electronic structure, and conductiv-

Density functional theory (DFT) calculations have been successfully utilized to understand the electronic structure of bioelectronic materials. Often, these studies make an assumption that the electronic structure of a subsystem, comprising of atoms forming anticipated charge carrier sites, can be partitioned and treated at the DFT level, while the electronic effects of the surrounding medium are described with a less computationally demanding model, e.g., by force fields^{33,35,36,45} or homology.^{39,44} Additionally, atomic vibrations associated with the subsystem and surrounding medium or bath can be incorporated in the theory to understand their role in reorganization energies, 35,45 structural properties, 36 or coupling of subsystem to the phonon bath associated with the environment. 40,42 However, the majority of studies neglect orbital delocalization outside of the subsystem partition, which can be important for coherent transport (through-bond tunneling), 33,46 and the impacts of the environment (screening, electronic delocalization on side chains), which can impact electronic coupling.35,42,45

In this work, we perform all-atom classical molecular dynamics (MD) and first-principles DFT calculations on a self-assembled antiparallel coiled-coil hexamer (ACC-Hex, see Figure 1), with the goal of understanding the underlying

physical features related to its conductivity. Hochbaum and coworkers³¹ have demonstrated efficient conductivity in ACC-Hex, constructed from de novo peptides.⁴⁷ The interleaving peptides are electrostatically bound in an antiparallel formation, forming a stable oligomer, which can stack endto-end and result in efficient carrier transport. By incorporating all atoms of the peptide bundle, as well as a solvation shell of explicit water, into the DFT simulation, we make no a priori assumptions about the physical or electronic structure, allowing for an unbiased perspective on its electronic structure. Our MD simulations predict that the peptides dimerize, with three strongly interwoven peptide pairs (dimers) that constitute the hexamer. DFT simulations, calculated within the hybrid implementation of the Perdew, Burke, and Erzenhoff functional (PBE0), 48-50 indicate that the hexamer is a large gap material with many nearly degenerate orbitals close to the band edges. The charge density associated with these orbitals is located near the phenylalanine rings as well as the charged residues. By extracting ~100 MD snapshots of one peptide dimer, we explore the role of finite temperature fluctuations in nuclei geometry and determine the dynamic localization and delocalization of orbitals.

2. METHODS

2.1. Molecular Dynamics Simulations. To obtain nuclear configurations for DFT, we conducted all-atom classical molecular dynamics simulations (MD) with the CHARMM36 force field. ^{51,52} We build our simulation using the CHARMM-GUI. ⁵³ The initial structure of the peptide was adapted from the published crystal structure (PDB code SEOJ), ⁴⁷ with protonation and deprotonation of residues to match physiological pH. To improve the MD, the terminuses of the peptides are kept as unmodified ammonium and carboxylate groups, retaining the total charge of the peptide; the iodophenylalanine residue (residue 21) is replaced by a phenylalanine. The LINCS algorithm is introduced to constrain chemical bonds involving hydrogen atoms. ⁵⁴ Ions (Na⁺ and Cl⁻) with a concentration of 150 mM are introduced to neutralize the system. Four different peptide models are introduced: peptide hexamer, peptide dimer, helical single

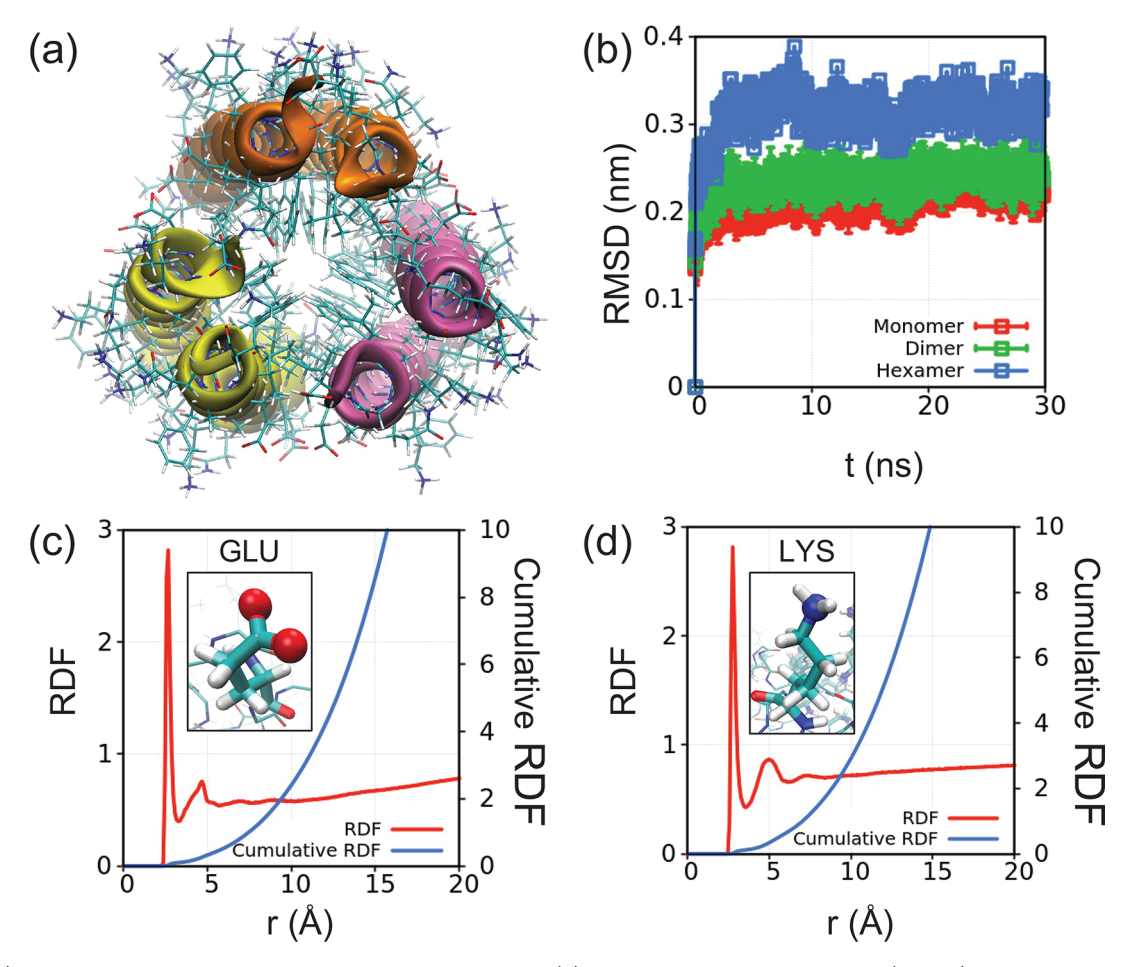


Figure 2. (a) Simulation snapshot of the hexamer as a trimer of dimers. (b) Root mean square displacement (RMSD) of six monomers (red), three dimers (green), and the hexamer (blue). Radial distribution function (red) and cumulative radial distribution function (blue) of oxygen atoms of water molecules to (c) oxygen of all Glu and (d) nitrogen of all Lys of the peptides.

peptide, and denatured single peptide. The hexamer, dimer, and single helical peptide are solvated with the TIP3P water model. To simulate denatured conformation of the peptide, we introduce helical peptide into a vacuum simulation box and run MD simulation with high temperature ($T=500~\rm K$) to transform the helical conformation into a denatured one.

We propagate these four models with the GROMACS simulation package. ⁵⁶ The hexamer, dimer, and single peptide models are solvated before performing 20 ns of equilibration MD; the equilibration is carried out with the solvent present. Subsequently, 50 ns of production MD simulations are performed postequilibration. Nose—Hoover thermostat and Parrinello—Rahman barostat are employed to maintain the temperature and pressure of the systems. ^{57–59} Except for the denatured peptide systems, all of our MD simulations are performed with a temperature of 303.15 K and pressure of 1 atm. The denatured peptide is simulated with the *NVT* ensemble with a temperature of 500 K. We integrate our simulations with 2 fs of the time step. From MD trajectories, we select 100 snapshots for each peptide models by performing clustering analysis. ⁶⁰

2.2. Density Functional Theory. Density functional theory $(DFT)^{61,62}$ calculations were performed using the Gaussian 16 software package.⁶³ The DFT exchange and correlation were described by the PBE0 hybrid functional with a cc-pVDZ double- ζ correlation-consistent basis set,⁶⁴ rotated and with redundant functions removed.⁶⁵ The peptide

nuclear geometry including a 2.8 Å thick explicit water shell is taken from MD for this all-atom DFT calculation. The triple-\(\zeta \) cc-pVTZ basis set resulted in only a slight HOMO-LUMO gap increase (0.1 eV) for a single helical peptide surrounded by explicit water, and thus, we use cc-pVDZ for subsequent calculations to reduce computational cost. We simulated a water environment surrounding the explicit waters using the C-PCM polarizable conductor calculation model. 66,67 Experimental measurements of electronic conductivity in the peptide fibers suggest no contribution from proton or counterionmediated transport, so we do not consider their effects in our calculations (see Supporting Information). The ACC-Hex molecule with a 2.8 Å thick explicit water shell consists of 4911 atoms. This procedure, when applied to different snapshots of the dimer from MD, results in different total numbers of electrons and atoms for different structures (1706-1847

Linear response time dependent DFT $(TDDFT)^{68-76}$ calculations within the Tamm-Dancoff approximation $(TDA)^{77}$ were performed to simulate the lowest 20 electronic excitations, corresponding to the optical absorption spectra of the denatured and α -helix single peptide structures, using Gaussian16's default Krylov subspace algorithm. 63

3. RESULTS

3.1. Structure of ACC-Hex. Figure 1a,b shows the structure of ACC-Hex as taken from a single snapshot of

MD simulations (after equilibration). The hexamer is composed of three peptide dimers that come together due to strong hydrophobic interaction between side chains of phenylalanine (Phe). There is no water inside the hexamer, and all water molecules stay on the outer shell. Figure 1c,d shows one snapshot of one of the peptide dimers. The pairs are interwoven, particularly around the ends, with Phe in place of the non-natural 4-iodopheylalanine in the original sequence. For both the full hexamer and peptide dimer, the Phe rings are interleaved along the long axis of the chain, suggesting a possible path for conductivity.

The MD simulations indicate that the hexamer bundle remains stable during the 500 ns of our simulation (Figure 2a). To quantify the structural integrity of the hexamer bundle, we calculate root-mean-square deviation (RMSD, Figure 2b) of six single chain monomers (red), three dimers of the peptide (green), and the hexamer bundle (blue) from their initial structure. The marginal difference between the RMSD of the monomer, the dimer, and the hexamer (0.1 nm) represents the structural integrity of the hexamer bundle. The hexamer is tightly bundled by the hydrophobic interaction between Phe and isoleucine (Ile) in the core. On the surface of the hexamer, charged residues (glutamic acid, Glu; lysine, Lys) are distributed, which recruit water molecules. By calculating the radial distribution function (RDF) and cumulative RDF of charged residues and oxygen atoms of the water molecules (Figure 2c,d), we quantify the hydration around the Glu and Lys residues. Sharp first peaks of RDFs represent the first hydration shell that formed around the Glu and Lys residues. By calculating the cumulative RDFs, we count the average number of water molecules around all Glu and Lys residues. Within 13 Å from Glu and Lys residues, approximately 5 oxygen atoms of correspondingly 5 water molecules are found.

3.2. Electronic Structure of ACC-Hex. We analyze the near-gap molecular orbital densities and the electronic density of states (DOS) at the band edges in Figures 3 and 4 in order to understand the bandgap, distribution of electronic states, and charge carrier delocalization.

As shown in Figure 3, the gap between occupied and unoccupied states (bandgap) is predicted to be 6.0 eV in ACC-Hex. The bandgap is similar to that predicted for a single

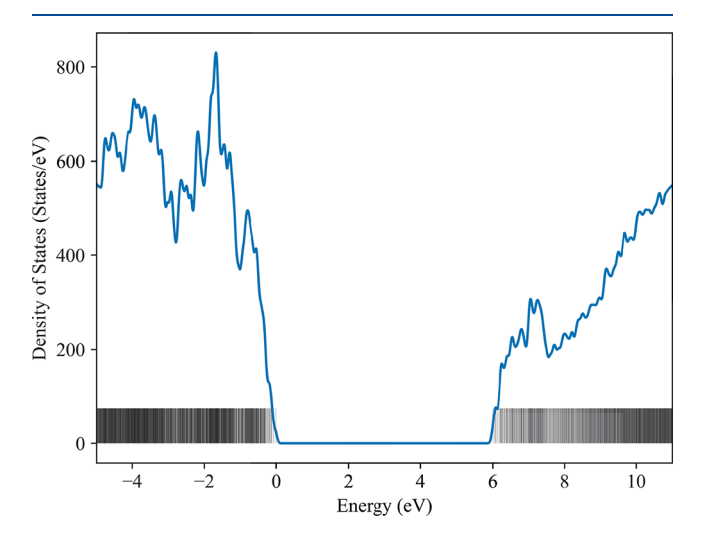


Figure 3. Density of states of ACC-Hex with 2.8 Å thick explicit water shell and the C-PCM solvation model beyond the explicit water shell. The black lines show the Kohn–Sham eigenstates.

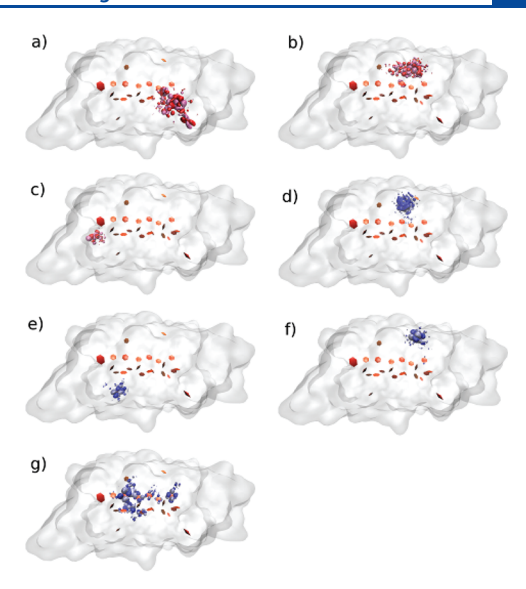


Figure 4. Orbital density associated with the (a) HOMO-2, (b) HOMO-1, (c) HOMO, (d) LUMO, (e) LUMO+1, (f) LUMO+2, and (g) LUMO+3 orbitals of ACC-Hex, showing significant density on or near one or more Phe rings. The isosurfaces are at value 0.01 and the white surface represents the van der Waal radii of the explicit water.

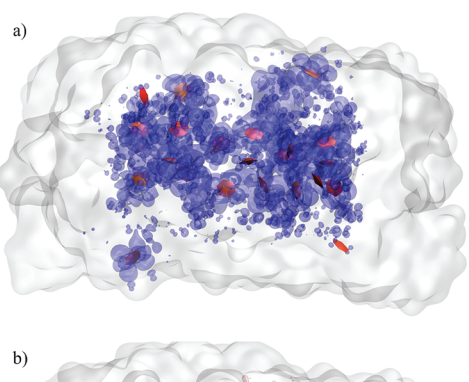
helical peptide or a single denatured peptide (5.8 and 5.7 eV, respectively), consistent with the experimentally and computationally derived structure in which interpeptide electronic interactions are noncovalent. These numbers are significantly larger than the experimental optical gap, which has been measured to be 4.8 eV for the denatured single peptide in acetonitrile (see Supporting Information Figure S3 for experimental spectrum). This discrepancy is partially due to the fact that the HOMO–LUMO gap is not a good representation of the optical gap. TDDFT simulations predict an optical gap of 5.0 and 5.1 eV for the helical and denatured peptide, respectively, in much better agreement with experiment (see Supporting Information Figure S3, the TDDFT-predicted spectrum compared with experiment).

The value of the bandgap and nature of orbitals are influenced by the approximations made in DFT. The predicted bandgap is significantly impacted by the DFT functional used: Considering a single helical peptide with an explicit water shell, the PBE0 gap is 5.8 eV, consistent with the hexamer. The PBE functional underestimates the gap at 3.1 eV due to the presence of significant self-interaction error, 78,79 while the long-range-corrected LCω-PBE functional predicts a gap of 10.6 eV. The overestimation of the gap by LC ω -PBE may be explained because of the lack of long-range screening in the functional. Another source of uncertainty in the electronic structure is our chosen solvation model. The bandgap in organic systems is highly dependent on the screening of the surrounding medium. The solvation model used in these calculations includes solvent screening; however, for the explicit shell of frozen water around the ACC-Hex, the dynamic screening due to the motion of water molecules is not described, overall underestimating the solvent screening and overestimating the bandgap. Without explicit water molecules present, including only implicit solvation to describe all solvation, the predicted bandgap is reduced by 1.4 to 4.4 eV, confirming the important role of accurate solvent screening. However, without explicit solvation, the density of states

(DOS) and nature of near-gap orbitals are not well-described. In particular, implicit solvent results in the HOMO on the negatively charged glutamic acid (Glu) residues, while the addition of the explicit water shell stabilizes the Glu residue, lowering the energy of the Glu-centered orbital such that there are now a significant number of near-gap occupied orbital states with density on Phe rings. The stabilization, missing from the implicit solvent correction but present with explicit water, is presumably due to explicit hydrogen-bonding and ion—dipole interaction of the lone pairs of Glu with the hydrogen of water. We note that the need for explicit solvation has been established in prior studies of the electronic structure of biomaterials.⁴⁴

The near-gap molecular orbitals are localized near one or more Phe, as well as on the Glu and Lys residues, and the peptide backbone, as shown in Figure 4a-g. For this particular structure extracted from MD, the molecular orbital associated with the highest occupied state (HOMO) is localized around the C-terminus of the peptide (Figure 4a). The HOMO-1 is centered on the amide backbone with some density on Phe16, one of the Phe rings within the core of ACC-Hex (Figure 4b). The HOMO-2 is centered on a different peptide backbone with significant delocalization over the solvent-exposed Phe21 residue and Phe23 within the core of the peptide (Figure 4c), with some additional delocalization over the core Phe9 of a different dimer. For the unoccupied states, the lowest unoccupied molecular orbital (LUMO) is Rydberg-like, nearest to a Lys10 residue and near the solvent-exposed Phe21 ring (Figure 4d). The LUMO+1, LUMO+2, and LUMO+3 are all centered on Phe rings. The LUMO+1 and LUMO+2 are localized on solvent exposed Phe21 rings (Figure 4e,f), while the LUMO+3 is delocalized over the Phe rings (Phe9, Phe16, and Phe23) within the core of one dimer, with some delocalization over Phe9 and Phe23 within the core of a different dimer subunit (Figure 4g). The HOMO-1 is separated by the HOMO by only 0.02 eV, while HOMO-2 and HOMO are separated by only 0.07 eV in energy. LUMO +1 and LUMO+2 are degenerate, separated by less than 0.001 eV in energy, while the LUMO+1 and LUMO+3 are separated by 0.04 eV. Thus, we would expect all of these orbitals to be important for conductivity.

As shown by the black lines at the bottom of Figure 3, there are many states that make up each peak of the occupied and unoccupied components of the DOS. While the HOMO and LUMO are expected to be most relevant for incoherent carrier transport for small organic molecules, larger supramolecular systems such as ACC-Hex may possess many nearly degenerate states that form a band of states relevant for conductivity. To better understand the impact of these states on conductivity, we consider whether states that are close in energy form a continuous distribution across the hexamer that would allow for band-like transport. For all near-gap states within 0.2 eV of the band edges, Figure 5 shows the average of their orbital density. For this structure of the hexamer extracted from MD, there are 16 occupied and 14 unoccupied states that lie within 0.2 eV of the HOMO and LUMO, respectively. As seen in Figure 5, the near-gap orbitals span along the length of the hexamer, delocalized over the Phe rings, peptide backbone, and Glu residues. This suggests that there is a path for conductivity of electrons and holes through the Phe rings, particularly for hole transport as the near-gap occupied orbitals extends from one end to the other of the hexamer. We note that these averaged orbitals are consistent with incoherent



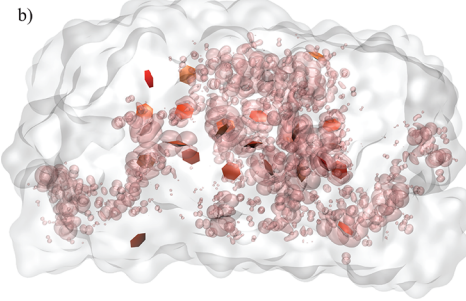


Figure 5. Extent of near-gap Kohn-Sham DFT orbital for ACC-Hex generated by averaging all occupied (unoccupied) orbitals within 0.2 eV of the HOMO (LUMO): (a) shows unoccupied states (blue) and (b) shows occupied states (red).

and mixed coherent—incoherent electron transport models, where delocalization of the adiabatic KS orbitals indicates strong electronic coupling between localized charge carrier sites.

3.3. Role of Room Temperature Vibrations on **Electronic Properties.** As noted in the Introduction, the role of atomic fluctuations at room temperature may also be important for describing the electronic structure of ACC-Hex, as has been shown for other bioelectronic materials. Notably, for MtrF (a protein complex with a chain of heme groups), thermally averaging the structure resulted in an increased electronic coupling by a factor 3 when compared to the T=0K structure. 36 Additionally, studies of studies of hypothetical G. sulfurreducens pilin protein structures, considering three aromatic rings explicitly with quantum mechanics, showed that atomic vibrations via molecular mechanics result in a timedependent change to the energy and ordering of molecular orbitals, 42 with the hole diffusivity dependence on dephasing being strongly dependent on geometry.³⁹ Here, we investigate the role of atomic vibrations on the energy and nature of neargap states in ACC-Hex.

As shown in Figure 4, the individual near-gap orbitals are mainly localized on a single dimer within the hexamer, with little cross-dimer delocalization. Thus, in order to limit computational cost, we focus the remainder of our analysis on a single dimer extracted from ACC-Hex (Figure 1c,d). Comparison of the DOS and frontier orbitals for one MD snapshot of this peptide dimer and the full hexamer indicates that the peptide dimer is a good description of the electronic structure (see Supporting Information). Additionally, by isolating a single dimer, we can better understand the role of vibrations by deconvoluting the vibrations from the full ACC-Hex

In order to describe the atomic vibrations induced by room temperature (T = 300 K), we extract structural samples from MD postequilibrium and study the electronic properties of

each snapshot via DFT. Figure 6 shows the superimposed DOS of 100 structures extracted from postequilibrium MD,

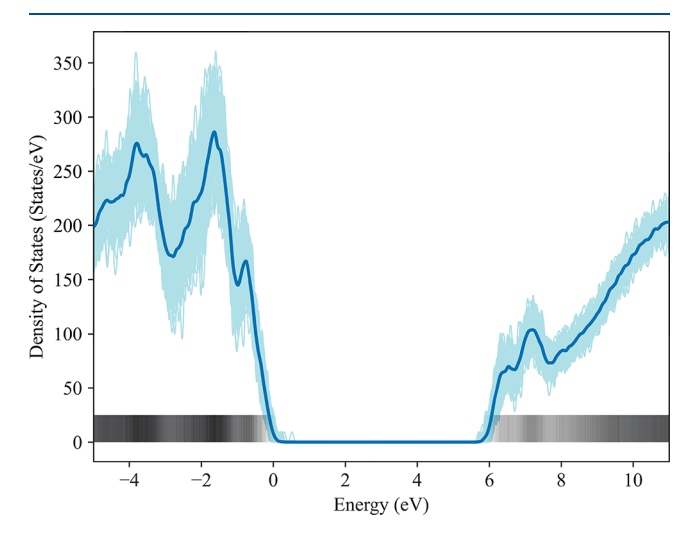


Figure 6. Superimposed density of states for 100 peptide dimers with with 2.8 Å thick explicit water shell (569–616 water molecules) and the C-PCM solvation model beyond the explicit water shell in light blue. A broadening of 0.1 eV full-width half-maximum was applied to each individual density of states plot. The average of the DOS is shown in bold, and the black lines show the eigenstates associated with all structures. The plots are shifted such that the average HOMO energy is set to zero.

with the average DOS outlined in bold. In general the DOS retains a similar shape between the different nuclear geometries. However, the value of the bandgap within the hundred structures varies by 0.83 eV, from 5.32 to 6.15 eV. The number of states that lie within 0.2 eV of the HOMO (LUMO) varies from 1 (1) to 15 (12) for the occupied (unoccupied) states with a median of 6 (5), both with a standard deviation of 3 states. A more detailed view of the variation in the density of states near the HOMO and LUMO is given by the histogram shown in the Supporting Information Figure S2; this variation suggests that thermal fluctuations will play a role in the electronic structure of ACC-Hex.

Having considered the change in energy distribution due to thermal effects, we next consider the change in spatial distribution of the near-gap KS orbitals, indicative of the spatial distribution of charge carrier sites and their coupling. Figure 7 shows the occupied and unoccupied molecular orbitals, averaging the magnitude of the orbitals that are within 0.2 eV of the band edges (HOMO and LUMO) for three representative snapshots from MD. The near-gap molecular orbitals vary from fully localized on one to two residues to delocalized over almost every Phe ring of the dimer. We speculate that temperature and disorder will be important for carrier transport. This is consistent with a flickering resonance electron transport as suggested Beratan and co-workers, 46,81 superexchange as suggested by Renaud and co-workers, 40,42 or both.

4. DISCUSSION

Our studies are the first all-atom classical MD approach coupled to first-principles electronic structure calculations of a large biomolecular assembly. By treatment of all electrons of the peptide bundle explicitly within the same level of theory, the full electronic structure of the ACC-Hex bundle is determined with no *a priori* assumption of the nature of conductivity in ACC-Hex.

The near-gap electronic structure of ACC-Hex is determined by not just the Phe rings but also other residues in the system and the backbone. There is no significant contribution of the orbitals of water to the near-gap electronic structure, implying that electron transfer to and from water to ACC-Hex is unlikely. The energy of occupied Glu-centered orbitals will be high because of its negative charge while unoccupied states near positively charged Lys will be lower in energy, making it energetically favorable for near-gap states to be localized on these residues. While screening due to solvent mitigates this effect (particularly with explicit water), the near-gap states maintain some degree of significant orbital density on the charged residues. For example, the HOMO of ACC-Hex has the highest orbital density on the carboxyl-terminus amide group but has significant electron density on the nearby negatively charged carbonyl group and the LUMO is

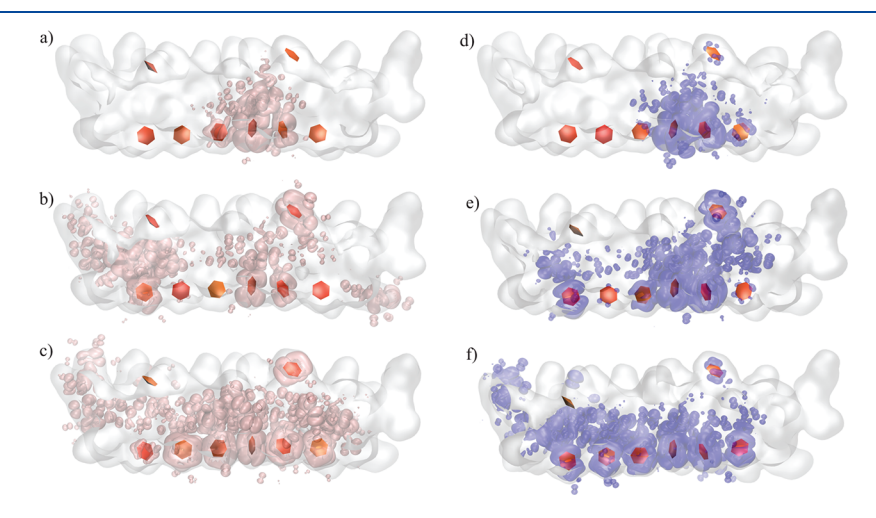


Figure 7. Extent of the Kohn–Sham orbitals computed as the average over all occupied (unoccupied) orbitals within 0.2 eV of the HOMO (LUMO) for structures corresponding to the minimum (a, d), median (b, e), and maximum (c, f) number of nearly degenerate states. Orbitals averaged over (a) one, (b) six, and (c) 14 occupied states. Orbitals averaged over (d) one, (e) five, and (f) 11 unoccupied states. Occupied states are shown in red and unoccupied states in blue.

delocalized over one Phe ring and a positively charged Lys. The LUMO+1 and LUMO+2 are on the aromatic Phe-21 residue that is close to another positively charged Lys group. The charged residues hence provide a different chemical environment for otherwise identical functional groups, creating energy gaps between functional groups that would otherwise be degenerate in energy. These energy gaps suggest a disordered landscape for electron or hole transport, suggesting a complex energy landscape similar to multiheme proteins. ^{33,35-37,45}

Additionally, the electronic structure is impacted by the charge states of residues. Under experimental conditions, the overall charge of ACC-Hex is +2 per peptide chain; hence, ACC-Hex is expected to be more easily reduced. For ACC-Hex, the highest energy occupied orbital with significant density on a Phe ring is the HOMO-2 at -6.947 eV (in contrast to Ru's reported value of -6.67 eV using the B3LYP functional) while the lowest energy unoccupied orbital localized on Phe is the LUMO+1, which is bound at -0.8550 eV. A significant number of the near-gap occupied orbitals have noticeable delocalization on the peptide backbone, where the localization of a hole could result in oxidative damage that may fragment or cross-link the backbone. 82 This is in contrast to the hypothetical structure of the G. sulfurreducens bacteria pilin peptide, 39,42,44 which contains two Phe and one tyrosine aromatic rings repeating on an uncoiled amide backbone, is negatively charged, and is predicted to support hole localization on Phe rings.

The spatial and energy distribution of the orbitals in the hexamer calculation aligns with the electronic structure description of conductivity models where thermal fluctuations are important. The energy distribution of the near-gap occupied and unoccupied states indicates many nearly degenerate states (see Figure 3). These states span respectively the length and width of the hexamer bundle (see Figure 5). In the superexchange and flickering resonance conductivity model, thermal fluctuations bring these near-degenerate orbitals into resonance, allowing for a charge carrier to tunnel between and over these orbitals, respectively.³² For ACC-Hex, the near-gap π -bonding orbitals that have significant component on the amide backbone have similar energy (-7.01 eV to -6.89 eV) to those associated with the aromatic rings of the peptide (-7.06 eV to -6.95 eV), suggesting the possibility of electron tunneling as suggested previously. 46 Additionally, the ability of the Phe residues pointing out of the bundle to rotate freely is consistent with vibration-induced conductivity along the outer edge of the hexamer. In particular, a few near-gap states are localized on outer bundle Phe and the thermal fluctuations of the Phe group can result in relatively smaller intermolecular distances and larger electronic couplings to support flickering resonance or band-like transport; this property is different from the more rigid heme-proteins.³⁵ Our studies of the conformation-dependence of the electronic structure shown in Figures 6 and 7 are consistent with such a picture.

5. CONCLUSIONS

In summary, we combined classical MD and DFT simulations to understand the physical and electronic structure of the de novo self-assembled peptide ACC-Hex. From classical MD, we determined that the peptides form interwoven dimers that self-assemble into a hexamer with a water shell screening the charges on residues. Applying DFT to all atoms of the hexamer

and the first solvation shell, we determined that the solvated hexamer has a gap of ~ 6 eV, with many nearly degenerate states near the gap that span end-to-end of the supramolecular structure that can potentially contribute to conductivity. Interestingly, we found participation of unexpected residue side chains and backbone in the near-gap occupied and unoccupied states. Additionally, by studying the electronic structure of 100 snapshots of the dimer taken from MD, we find that the character of the near-gap orbitals is sensitive to thermal vibrations, suggesting time- and temperature-dependence of the electron transport parameters. These findings provide a new perspective on the properties of amino acid-based biomaterials and on protein electronic structure calculations.

ASSOCIATED CONTENT

Supporting Information

The Supporting Information is available free of charge at https://pubs.acs.org/doi/10.1021/acs.jpcb.2c02346.

Impact of explicit versus implicit solvation on the electronic structure of ACC-Hex, analysis of the electronic structure of the dimer with atomic fluctuations, experimental and calculated optical absorption spectra of the denatured peptide, and measured conductivity of the peptides in aqueous solution (PDF)

AUTHOR INFORMATION

Corresponding Author

Sahar Sharifzadeh — Department of Electrical and Computer Engineering, Boston University, Boston, Massachusetts 02215, United States; Division of Materials Science and Engineering, Department of Physics, and Department of Chemistry, Boston University, Boston, Massachusetts 02215, United States; orcid.org/0000-0003-4215-4668; Email: ssharifz@bu.edu

Authors

D. Kirk Lewis – Department of Electrical and Computer Engineering, Boston University, Boston, Massachusetts 02215, United States

Younghoon Oh – Department of Chemistry, Boston University, Boston, Massachusetts 02215, United States

Luke Nambi Mohanam — Department of Electrical and Computer Engineering, Boston University, Boston, Massachusetts 0221S, United States

Michał Wierzbicki – Department of Materials Science and Engineering, University of California Irvine, Irvine, California 92697, United States; orcid.org/0000-0002-9217-634X

Nicole L. Ing — Department of Materials Science and Engineering, University of California Irvine, Irvine, California 92697, United States

Lei Gu – Department of Physics, University of California Irvine, Irvine, California 92697, United States

Allon Hochbaum – Department of Materials Science and Engineering, University of California Irvine, Irvine, California 92697, United States; Department of Chemistry, Department of Molecular Biology and Biochemistry, and Department of Chemical and Biomolecular Engineering, University of California Irvine, Irvine, California 92697, United States; orcid.org/0000-0002-5377-8065

- Ruqian Wu Department of Physics, University of California Irvine, Irvine, California 92697, United States; orcid.org/ 0000-0002-6156-7874
- Qiang Cui Department of Chemistry and Division of Materials Science and Engineering, Boston University, Boston, Massachusetts 02215, United States; orcid.org/0000-0001-6214-5211

Complete contact information is available at: https://pubs.acs.org/10.1021/acs.jpcb.2c02346

Notes

The authors declare no competing financial interest.

ACKNOWLEDGMENTS

This research was primarily supported by the National Science Foundation Materials Research Science and Engineering Center program through the UC Irvine Center for Complex and Active Materials (Grant DMR-2011967). Q.C. and Y.O. were supported by NIH Grant R35-GM141930. M.W. and A.H. acknowledge additional support from AFOSR Grant FA9550-19-1-0380. We also acknowledge computational resources from the Extreme Science and Engineering Discovery Environment (XSEDE⁸³), which is supported by NSF Grant ACI-1548562, specifically the Bridges-2 system which is supported by NSF Award ACI-1928147 at the Pittsburgh Supercomputing Center (PSC), and the Shared Computing Cluster which is administered by Boston University's Research Computing Services (URL: www.bu.edu/tech/support/research/).

REFERENCES

- (1) Wang, F.; Gu, Y.; O'Brien, J. P.; Yi, S. M.; Yalcin, S. E.; Srikanth, V.; Shen, C.; Vu, D.; Ing, N. L.; Hochbaum, A. I.; et al. Structure of Microbial Nanowires Reveals Stacked Hemes that Transport Electrons over Micrometers. *Cell* **2019**, *177*, 361–369.e10.
- (2) Yalcin, S. E.; O'Brien, J. P.; Gu, Y.; Reiss, K.; Yi, S. M.; Jain, R.; Srikanth, V.; Dahl, P. J.; Huynh, W.; Vu, D.; et al. Electric field stimulates production of highly conductive microbial OmcZ nanowires. *Nat. Chem. Biol.* **2020**, *16*, 1136–1142.
- (3) Boschker, H. T. S.; Cook, P. L. M.; Polerecky, L.; Eachambadi, R. T.; Lozano, H.; Hidalgo-Martinez, S.; Khalenkow, D.; Spampinato, V.; Claes, N.; Kundu, P.; et al. Efficient long-range conduction in cable bacteria through nickel protein wires. *Nat. Commun.* **2021**, *12*, 3996.
- (4) Edwards, M. J.; White, G. F.; Butt, J. N.; Richardson, D. J.; Clarke, T. A. The Crystal Structure of a Biological Insulated Transmembrane Molecular Wire. *Cell* **2020**, *181*, 665–673.
- (5) Agostini, F.; Völler, J.-S.; Koksch, B.; Acevedo-Rocha, C. G.; Kubyshkin, V.; Budisa, N. Biocatalysis with Unnatural Amino Acids: Enzymology Meets Xenobiology. *Angew. Chem., Int. Ed.* **2017**, *56*, 9680–9703.
- (6) Young, T. S.; Schultz, P. G. Beyond the canonical 20 amino acids: expanding the genetic lexicon. *J. Biol. Chem.* **2010**, 285, 11039–11044.
- (7) Wang, L.; Xie, J.; Schultz, P. G. Expanding the Genetic Code. Annu. Rev. Biophys. Biomol. Struct. 2006, 35, 225-249.
- (8) Ravikumar, Y.; Nadarajan, S. P.; Hyeon Yoo, T.; Lee, C.-S.; Yun, H. Incorporating unnatural amino acids to engineer biocatalysts for industrial bioprocess applications. *Biotechnology Journal* **2015**, *10*, 1862–1876.
- (9) Zelzer, M.; Todd, S. J.; Hirst, A. R.; McDonald, T. O.; Ulijn, R. V. Enzyme responsive materials: design strategies and future developments. *Biomaterials Science* **2013**, *1*, 11–39.
- (10) Kumar, M.; Ing, N. L.; Narang, V.; Wijerathne, N. K.; Hochbaum, A. I.; Ulijn, R. V. Amino-acid-encoded biocatalytic self-

- assembly enables the formation of transient conducting nanostructures. *Nature Chem.* **2018**, *10*, 696–703.
- (11) Brown, J. E.; Moreau, J. E.; Berman, A. M.; McSherry, H. J.; Coburn, J. M.; Schmidt, D. F.; Kaplan, D. L. Shape Memory Silk Protein Sponges for Minimally Invasive Tissue Regeneration. *Adv. Healthcare Mater.* **2017**, *6*, 1600762.
- (12) Bayrak, A.; Prüger, P.; Stock, U. A.; Seifert, M. Absence of Immune Responses with Xenogeneic Collagen and Elastin. *Tissue Engineering Part A* **2013**, *19*, 1592–1600.
- (13) DeLustro, F.; Dasch, J.; Keefe, J.; Ellingsworth, L. Immune responses to allogeneic and xenogeneic implants of collagen and collagen derivatives. *Clin. Orthop. Relat. Res.* **1990**, *260*, *263*–279.
- (14) Turabee, M. H.; Thambi, T.; Lym, J. S.; Lee, D. S. Bioresorbable polypeptide-based comb-polymers efficiently improves the stability and pharmacokinetics of proteins in vivo. *Biomater. Sci.* **2017**, *5*, 837–848.
- (15) Tao, H.; Hwang, S.-W.; Marelli, B.; An, B.; Moreau, J. E.; Yang, M.; Brenckle, M. A.; Kim, S.; Kaplan, D. L.; Rogers, J. A.; et al. Silk-based resorbable electronic devices for remotely controlled therapy and in vivo infection abatement. *Proc. Natl. Acad. Sci. U. S. A.* **2014**, *111*, 17385–17389.
- (16) Rajkhowa, R.; Hu, X.; Tsuzuki, T.; Kaplan, D. L.; Wang, X. Structure and Biodegradation Mechanism of Milled Bombyx mori Silk Particles. *Biomacromolecules* **2012**, *13*, 2503–2512.
- (17) Giano, M. C.; Pochan, D. J.; Schneider, J. P. Controlled biodegradation of Self-assembling -hairpin Peptide hydrogels by proteolysis with matrix metalloproteinase-13. *Biomaterials* **2011**, *32*, 6471–6477.
- (18) Shi, J.; Schellinger, J. G.; Pun, S. H. Engineering biodegradable and multifunctional peptide-based polymers for gene delivery. *J. Biol. Eng.* **2013**, *7*, 25.
- (19) Fu, J.; Cai, K.; Johnston, S. A.; Woodbury, N. W. Exploring Peptide Space for Enzyme Modulators. *J. Am. Chem. Soc.* **2010**, *132*, 6419–6424.
- (20) Fu, J.; Reinhold, J.; Woodbury, N. W. Peptide-Modified Surfaces for Enzyme Immobilization. *PLoS One* **2011**, *6*, e18692.
- (21) Wei, G.; Yao, M.; Wang, Y.; Zhou, C.; Wan, D.; Lei, P.; Wen, J.; Lei, H.; Dong, D. Promotion of peripheral nerve regeneration of a peptide compound hydrogel scaffold. *Int. J. Nanomed.* **2013**, *8*, 3217–3225.
- (22) Wei, G.; Wang, L.; Dong, D.; Teng, Z.; Shi, Z.; Wang, K.; An, G.; Guan, Y.; Han, B.; Yao, M.; et al. Promotion of cell growth and adhesion of a peptide hydrogel scaffold via mTOR/cadherin signaling. *Journal of Cellular Physiology* **2018**, 233, 822–829.
- (23) Wang, X.-m.; Qiao, L.; Horii, A. Screening of functionalized self-assembling peptide nanofiber scaffolds with angiogenic activity for endothelial cell growth. *Progress in Natural Science: Materials International* **2011**, 21, 111–116.
- (24) De Santis, E.; Ryadnov, M. G. Peptide self-assembly for nanomaterials: the old new kid on the block. *Chem. Soc. Rev.* **2015**, *44*, 8288–8300.
- (25) Bai, Y.; Luo, Q.; Liu, J. Protein self-assembly via supramolecular strategies. *Chem. Soc. Rev.* **2016**, *45*, 2756–2767.
- (26) Liu, J.; Xie, C.; Dai, X.; Jin, L.; Zhou, W.; Lieber, C. M. Multifunctional three-dimensional macroporous nanoelectronic networks for smart materials. *Proc. Natl. Acad. Sci. U. S. A.* **2013**, *110*, 6694–6699.
- (27) Duan, X.; Gao, R.; Xie, P.; Cohen-Karni, T.; Qing, Q. C.; Choe, H. S.; Tian, B.; Jiang, X.; Lieber, C. M. Intracellular recordings of action potentials by an extracellular nanoscale field-effect transistor. *Nat. Nanotechnol.* **2012**, *7*, 174–179.
- (28) Amir Parviz, B.; Ryan, D.; Whitesides, G. Using self-assembly for the fabrication of nano-scale electronic and photonic devices. *IEEE Trans. Adv. Packag.* **2003**, *26*, 233–241.
- (29) Gray, H. B.; Winkler, J. R. Long-range electron transfer. *Proc. Natl. Acad. Sci. U. S. A.* **2005**, *102*, 3534–3539.
- (30) Winkler, J. R.; Gray, H. B. Electron Flow through Metalloproteins. *Chem. Rev.* **2014**, *114*, 3369–3380.

- (31) Ing, N. L.; Nusca, T. D.; Hochbaum, A. I. Geobacter sulfurreducens pili support ohmic electronic conduction in aqueous solution. *Phys. Chem. Chem. Phys.* **2017**, *19*, 21791–21799.
- (32) Ing, N. L.; El-Naggar, M. Y.; Hochbaum, A. I. Going the Distance: Long-Range Conductivity in Protein and Peptide Bioelectronic Materials. *J. Phys. Chem. B* **2018**, *122*, 10403–10423.
- (33) Futera, Z.; Ide, I.; Kayser, B.; Garg, K.; Jiang, X.; Van Wonderen, J. H.; Butt, J. N.; Ishii, H.; Pecht, I.; Sheves, M.; et al. Coherent Electron Transport across a 3 nm Bioelectronic Junction Made of Multi-Heme Proteins. *J. Phys. Chem. Lett.* **2020**, *11*, 9766–9774.
- (34) Warren, J. J.; Ener, M. E.; Vlček, A.; Winkler, J. R.; Gray, H. B. Electron hopping through proteins. *Coord. Chem. Rev.* **2012**, 256, 2478–2487.
- (35) Jiang, X.; Van Wonderen, J. H.; Butt, J. N.; Edwards, M. J.; Clarke, T. A.; Blumberger, J. Which Multi-Heme Protein Complex Transfers Electrons More Efficiently? Comparing MtrCAB from Shewanella with OmcS from Geobacter. *J. Phys. Chem. Lett.* **2020**, *11*, 9421–9425.
- (36) Breuer, M.; Rosso, K. M.; Blumberger, J. Electron flow in multiheme bacterial cytochromes is a balancing act between heme electronic interaction and redox potentials. *Proc. Natl. Acad. Sci. U. S. A.* **2014**, *111*, 611–616.
- (37) Agam, Y.; Nandi, R.; Kaushansky, A.; Peskin, U.; Amdursky, N. The porphyrin ring rather than the metal ion dictates long-range electron transport across proteins suggesting coherence-assisted mechanism. *Proc. Natl. Acad. Sci. U.S.A.* **2020**, *117*, 32260–32266.
- (38) Eshel, Y.; Peskin, U.; Amdursky, N. Coherence-assisted electron diffusion across the multi-heme protein-based bacterial nanowire. *Nanotechnology* **2020**, *31*, 314002.
- (39) Ru, X.; Zhang, P.; Beratan, D. N. Assessing Possible Mechanisms of Micrometer-Scale Electron Transfer in Heme-Free Geobacter sulfurreducens Pili. *J. Phys. Chem. B* **2019**, *123*, 5035–5047.
- (40) Renaud, N.; Berlin, Y. A.; Lewis, F. D.; Ratner, M. A. Between Superexchange and Hopping: An Intermediate Charge-Transfer Mechanism in Poly(A)-Poly(T) DNA Hairpins. *J. Am. Chem. Soc.* **2013**, *135*, 3953–3963.
- (41) Beratan, D. N.; Betts, J. N.; Onuchic, J. N. Protein electron transfer rates set by the bridging secondary and tertiary structure. *Science* **1991**, 252, 1285–1288.
- (42) Mezzina Freitas, L. P.; Feliciano, G. T. Atomic and Electronic Structure of Pilus from Geobacter sulfurreducens through QM/MM Calculations: Evidence for Hole Transfer in Aromatic Residues. *J. Phys. Chem. B* **2021**, *125*, 8305–8312.
- (43) Malvankar, N. S.; Yalcin, S. E.; Tuominen, M. T.; Lovley, D. R. Visualization of charge propagation along individual pili proteins using ambient electrostatic force microscopy. *Nat. Nanotechnol.* **2014**, *9*, 1012–1017.
- (44) Feliciano, G. T.; Da Silva, A. J.; Reguera, G.; Artacho, E. Molecular and electronic structure of the peptide subunit of Geobacter sulfurreducens conductive pili from first principles. *J. Phys. Chem. A* **2012**, *116*, 8023–8030.
- (45) Jiang, X.; Burger, B.; Gajdos, F.; Bortolotti, C.; Futera, Z.; Breuer, M.; Blumberger, J. Kinetics of trifurcated electron flow in the decaheme bacterial proteins MtrC and MtrF. *Proc. Natl. Acad. Sci. U. S. A.* **2019**, *116*, 3425–3430.
- (46) Beratan, D. N. Why Are DNA and Protein Electron Transfer So Different? *Annu. Rev. Phys. Chem.* **2019**, *70*, 71–97.
- (47) Spencer, R. K.; Hochbaum, A. I. X-ray Crystallographic Structure and Solution Behavior of an Antiparallel Coiled-Coil Hexamer Formed by de Novo Peptides. *Biochemistry* **2016**, *55*, 3214–3223.
- (48) Perdew, J. P.; Burke, K.; Ernzerhof, M. Generalized Gradient Approximation Made Simple. *Phys. Rev. Lett.* **1996**, 77, 3865–3868.
- (49) Perdew, J. P.; Burke, K.; Ernzerhof, M. Generalized Gradient Approximation Made Simple. *Phys. Rev. Lett.* **1997**, *78*, 1396–1396.

- (50) Adamo, C.; Barone, V. Toward reliable density functional methods without adjustable parameters: The PBE0 model. *J. Chem. Phys.* **1999**, *110*, 6158–6170.
- (51) Huang, J.; MacKerell, A. D. CHARMM36 all-atom additive protein force field: Validation based on comparison to NMR data. *J. Comput. Chem.* **2013**, *34*, 2135–2145.
- (52) Klauda, J. B.; Venable, R. M.; Freites, J. A.; O'Connor, J. W.; Tobias, D. J.; Mondragon-Ramirez, C.; Vorobyov, I.; MacKerell, A. D.; Pastor, R. W. Update of the CHARMM All-Atom Additive Force Field for Lipids: Validation on Six Lipid Types. *J. Phys. Chem. B* **2010**, 114, 7830–7843.
- (53) Jo, S.; Kim, T.; Iyer, V. G.; Im, W. CHARMM-GUI: A webbased graphical user interface for CHARMM. *J. Comput. Chem.* **2008**, 29, 1859–1865.
- (54) Hess, B.; Bekker, H.; Berendsen, H. J. C.; Fraaije, J. G. E. M. LINCS: A linear constraint solver for molecular simulations. *J. Comput. Chem.* **1997**, *18*, 1463–1472.
- (55) Jorgensen, W. L.; Chandrasekhar, J.; Madura, J. D.; Impey, R. W.; Klein, M. L. Comparison of simple potential functions for simulating liquid water. *J. Chem. Phys.* **1983**, *79*, 926–935.
- (56) Van Der Spoel, D.; Lindahl, E.; Hess, B.; Groenhof, G.; Mark, A. E.; Berendsen, H. J. C. GROMACS: fast, flexible, and free. *J. Comput. Chem.* **2005**, 26, 1701–1718.
- (57) Parrinello, M.; Rahman, A. Polymorphic transitions in single crystals: A new molecular dynamics method. *J. Appl. Phys.* **1981**, *52*, 7182–7190.
- (58) Nosé, S. A unified formulation of the constant temperature molecular dynamics methods. *J. Chem. Phys.* **1984**, *81*, 511.
- (59) Hoover, W. G. Canonical dynamics: equilibrium phase-space distributions. *Phys. Rev. A* **1985**, *31*, 1695–1697.
- (60) Shortle, D.; Simons, K. T.; Baker, D. Clustering of low-energy conformations near the native structures of small proteins. *Proc. Natl. Acad. Sci. U. S. A.* **1998**, 95, 11158–11162.
- (61) Hohenberg, P.; Kohn, W. Inhomogeneous Electron Gas. *Phys. Rev.* **1964**, *136*, B864–B871.
- (62) Kohn, W.; Sham, L. J. Self-Consistent Equations Including Exchange and Correlation Effects. *Phys. Rev.* **1965**, *140*, A1133–A1138.
- (63) Frisch, M. J.; Trucks, G. W.; Schlegel, H. B.; Scuseria, G. E.; Robb, M. A.; Cheeseman, J. R.; Scalmani, G.; Barone, V.; Petersson, G. A.; Nakatsuji, H.; et al. *Gaussian 16*, revision C.01; Gaussian Inc.: Wallingford, CT, 2016.
- (64) Dunning, T. H. Gaussian basis sets for use in correlated molecular calculations. I. The atoms boron through neon and hydrogen. *J. Chem. Phys.* **1989**, *90*, 1007–1023.
- (65) Davidson, E. R. Comment on "Comment on Dunning's correlation-consistent basis sets. *Chem. Phys. Lett.* **1996**, 260, 514–518.
- (66) Barone, V.; Cossi, M. Quantum Calculation of Molecular Energies and Energy Gradients in Solution by a Conductor Solvent Model. *J. Phys. Chem. A* **1998**, *102*, 1995–2001.
- (67) Cossi, M.; Rega, N.; Scalmani, G.; Barone, V. Energies, structures, and electronic properties of molecules in solution with the C-PCM solvation model. *J. Comput. Chem.* **2003**, *24*, 669–681.
- (68) Bauernschmitt, R.; Ahlrichs, R. Treatment of electronic excitations within the adiabatic approximation of time dependent density functional theory. *Chem. Phys. Lett.* **1996**, 256, 454–464.
- (69) Casida, M. E.; Jamorski, C.; Casida, K. C.; Salahub, D. R. Molecular excitation energies to high-lying bound states from time-dependent density-functional response theory: Characterization and correction of the time-dependent local density approximation ionization threshold. *J. Chem. Phys.* 1998, 108, 4439–4449.
- (70) Stratmann, R. E.; Scuseria, G. E.; Frisch, M. J. An efficient implementation of time-dependent density-functional theory for the calculation of excitation energies of large molecules. *J. Chem. Phys.* **1998**, *109*, 8218–8224.
- (71) Van Caillie, C.; Amos, R. D. Geometric derivatives of excitation energies using SCF and DFT. *Chem. Phys. Lett.* **1999**, *308*, 249–255.

- (72) Van Caillie, C.; Amos, R. D. Geometric derivatives of density functional theory excitation energies using gradient-corrected functionals. *Chem. Phys. Lett.* **2000**, 317, 159–164.
- (73) Furche, F.; Ahlrichs, R. Adiabatic time-dependent density functional methods for excited state properties. *J. Chem. Phys.* **2002**, 117, 7433–7447.
- (74) Scalmani, G.; Frisch, M. J.; Mennucci, B.; Tomasi, J.; Cammi, R.; Barone, V. Geometries and properties of excited states in the gas phase and in solution: Theory and application of a time-dependent density functional theory polarizable continuum model. *J. Chem. Phys.* **2006**, *124*, 094107.
- (75) Adamo, C.; Jacquemin, D. The calculations of excited-state properties with Time-Dependent Density Functional Theory. *Chem. Soc. Rev.* **2013**, 42, 845–856.
- (76) Laurent, A. D.; Adamo, C.; Jacquemin, D. Dye chemistry with time-dependent density functional theory. *Phys. Chem. Chem. Phys.* **2014**, *16*, 14334–14356.
- (77) Hirata, S.; Head-Gordon, M. Time-dependent density functional theory within the Tamm-Dancoff approximation. *Chem. Phys. Lett.* **1999**, 314, 291–299.
- (78) Perdew, J. P. Density functional theory and the band gap problem. *Int. J. Quantum Chem.* **1985**, 28, 497–523.
- (79) Ruiz, E.; Alvarez, S.; Cano, J.; Polo, V. About the calculation of exchange coupling constants using density-functional theory: The role of the self-interaction error. *J. Chem. Phys.* **2005**, *123*, 164110.
- (80) Sharifzadeh, S.; Biller, A.; Kronik, L.; Neaton, J. B. Quasiparticle and optical spectroscopy of the organic semiconductors pentacene and PTCDA from first principles. *Phys. Rev. B* **2012**, *85*, 125307.
- (81) Zhang, Y.; Liu, C.; Balaeff, A.; Skourtis, S. S.; Beratan, D. N. Biological charge transfer via flickering resonance. *Proc. Natl. Acad. Sci. U. S. A.* **2014**, *111*, 10049–10054.
- (82) Davies, M. J. Protein oxidation and peroxidation. *Biochemical journal* **2016**, 473, 805–825.
- (83) Towns, J.; Cockerill, T.; Dahan, M.; Foster, I.; Gaither, K.; Grimshaw, A.; Hazlewood, V.; Lathrop, S.; Lifka, D.; Peterson, G. D.; et al. XSEDE: Accelerating Scientific Discovery. *Computing in Science Engineering* **2014**, *16*, 62–74.

☐ Recommended by ACS

Folding Coarse-Grained Oligomer Models with PyRosetta

Theodore L. Fobe, Michael R. Shirts, et al.

SEPTEMBER 30, 2022

JOURNAL OF CHEMICAL THEORY AND COMPUTATION

READ 🗹

Peptide-RNA Coacervates as a Cradle for the Evolution of Folded Domains

Manas Seal, Daniella Goldfarb, et al.

JULY 29, 2022

JOURNAL OF THE AMERICAN CHEMICAL SOCIETY

READ 🗹

Assembly of π -Stacking Helical Peptides into a Porous and Multivariable Proteomimetic Framework

Sherrie L. Heinz-Kunert, Andy I. Nguyen, et al.

APRIL 07, 2022

JOURNAL OF THE AMERICAN CHEMICAL SOCIETY

READ 🗹

Self-Assembled Fullerene Nanostructures for Mimicking and Understanding of Natural Enzymes

Zeynep Demirsoy and Gulcihan Gulseren

SEPTEMBER 16, 2022

ACS APPLIED NANO MATERIALS

READ 🗹

Get More Suggestions >